

Nonreciprocal piezoelectric metamaterial framework and circuit strategiesChristopher Sugino,^{1,*} Massimo Ruzzene,² and Alper Erturk¹¹*G.W. Woodruff School of Mechanical Engineering, Georgia Institute of Technology, Atlanta, Georgia 30332, USA*²*Department of Mechanical Engineering, University of Colorado Boulder, Boulder, Colorado 80309, USA*

(Received 18 March 2020; revised 2 June 2020; accepted 17 June 2020; published 6 July 2020)

Recent research has shown that a proper spatiotemporal modulation of material properties (i.e., mass density or stiffness) can break reciprocity for elastic waves; however, such concepts are challenging to implement experimentally in mechanical waveguides. Piezoelectric metamaterials offer the possibility of parameter modification via electrical circuitry, constituting a convenient platform for spatiotemporal modulation. We introduce a fully coupled electromechanical framework and circuit strategies to enable nonreciprocal piezoelectric metamaterials using various schemes that include capacitive and inductive shunts as well as smooth modulation and nonsmooth switching. The high-fidelity framework presented herein does not rely on the assumption of simplified effective material property representation, and can be used to explore and predict the complete dynamics of the modulated system, accounting for full-system stability, circuit limitations, and more complex modulation schemes. A set of results is presented based on nonreciprocal configurations that illustrate potential implementation schemes, and demonstrate the versatility of piezoelectric materials for the design of truly integrated acoustic/elastic wave devices featuring nonreciprocal transmission.

DOI: [10.1103/PhysRevB.102.014304](https://doi.org/10.1103/PhysRevB.102.014304)**I. INTRODUCTION**

In conventional time-invariant materials, the principle of *reciprocity* states that waves will propagate symmetrically between two points, such that the source and receiver are interchangeable. Research has been shown across a variety of physical domains that reciprocity can be broken through nonlinearity or the introduction of directional bias (i.e., by relaxing the time-invariant constraint), with numerous potential applications in wave isolation [1,2], such as blocking reflections from returning to a source.

Numerous techniques have been proposed to break wave reciprocity in elastic or acoustic wave devices. Introducing strong nonlinearity into a medium can break reciprocity through frequency conversion [3–5], but this technique is fundamentally amplitude dependent and dramatically changes the spectral content of the input wave. Linear techniques typically rely on the use of active components, either by introducing a form of directional bias [6] or other control techniques [7–9]. In recent years, research interest has grown in so-called spatiotemporal periodic structures [10–15], or structures whose material properties vary periodically in both space and time. Trainiti and Ruzzene [10] demonstrated numerically that rods and beams with spatiotemporal periodic stiffness and density exhibit nonreciprocal wave propagation. Nassar *et al.* [13] investigated a modulated phononic crystal using a Willis model [16], but noted that experimental realization of such a structure poses a significant challenge. In another work, Nassar *et al.* [14] also investigated a modulated locally resonant spring-mass chain using a perturbation

method, obtaining directional band gaps by modulating the local resonator coupling stiffness. Vila *et al.* [12] developed a generalized Bloch procedure for analyzing elastic waves in modulated discrete spring-mass systems. Riva *et al.* [17] developed a similar plane-wave expansion approach to obtain the dispersion of modulated systems.

The preceding research in spatiotemporal periodic structures relies upon a material or component whose material properties are strongly modulated periodically in time, something that is challenging to realize experimentally. Several concepts have been proposed to achieve this, such as magnetoelastic polymers [18] or piezoelectric media [19]. Still, there has been limited experimental realization of reciprocity-breaking elastic metamaterials, suggesting that more thorough analysis is required to understand the dynamics of these modulated systems. To address this issue, this work develops a fully coupled electromechanical modeling framework for piezoelectric metamaterials with time-varying shunt circuitry. Similar to direct modulation of material properties, appropriate modulation of shunt circuit parameters can break elastic wave reciprocity. Importantly, time-varying circuit components are straightforward to obtain in real systems, e.g., through the use of electrical switches or digital control and synthetic impedance [20]. Additionally, the use of a complete circuit model enables analysis of more complex material property modulation, such as modulation with frequency-dependent effective properties.

II. GENERALIZED PLANE-WAVE EXPANSION METHOD FOR SPATIOTEMPORAL PERIODIC PIEZOELECTRIC METAMATERIALS

Consider an infinite piezoelectric bimorph plate made from a two-dimensional Bravais lattice of unit cells, each with a

* Author to whom correspondence should be addressed: csugino@gatech.edu

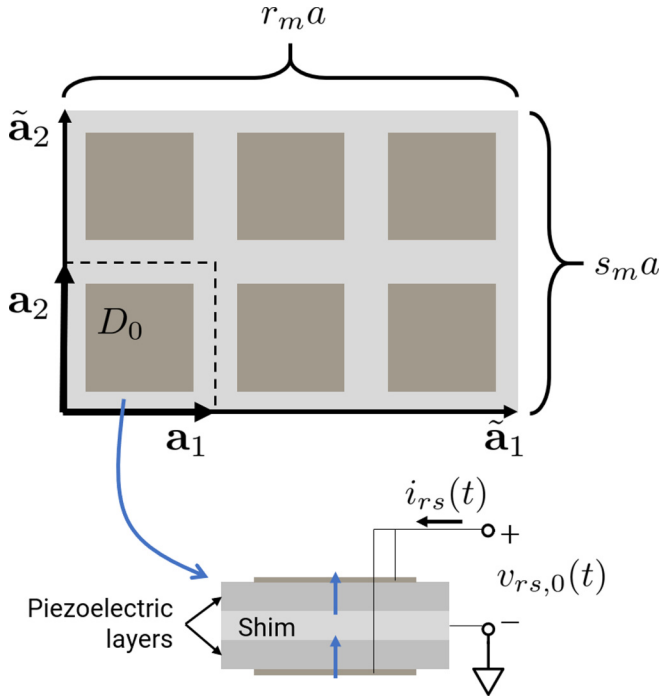


FIG. 1. Schematic for the unit cell of the piezoelectric bimorph plate. The system has a primitive unit cell (shown by the dashed line) with lattice vectors \mathbf{a}_1 and \mathbf{a}_2 . Circuit modulation in space extends the periodic unit cell to the supercell (here with $r_m = 3$, $s_m = 2$) which has lattice vectors $\tilde{\mathbf{a}}_1$ and $\tilde{\mathbf{a}}_2$.

single electrode pair, with lattice vectors \mathbf{a}_1 and \mathbf{a}_2 , shown schematically in Fig. 1. The bimorph plate consists of two transversely isotropic piezoelectric layers sandwiching a central shim, which is assumed to be an ideal conductor. The two piezoelectric layers are assumed to be transversely isotropic (e.g., piezoceramics) and poled in the same direction through the thickness. A periodic unit cell is introduced via electrode segmentation on the external faces of the plate (alternatively piezoelectric patches can be segmented), with each unit cell comprising one symmetric pair of opposing electrodes, electrically connected to each other for parallel wire operation.

The governing equations for this system are given by [21]

$$\left(D^E \nabla^4 + m_p \frac{\partial^2}{\partial t^2} \right) w(\mathbf{P}, t) - \vartheta \sum_{r,s} v_{rs,0}(t) \nabla^2 d(\mathbf{P} - \mathbf{P}_{rs}) = 0, \quad (1)$$

$$C_p \dot{v}_{rs,0}(t) + \vartheta \frac{d}{dt} \int_D d(\mathbf{P} - \mathbf{P}_{rs}) \nabla^2 w(\mathbf{P}, t) dD = i_{rs}(t), \quad (2)$$

where $w(\mathbf{P}, t)$, D^E , m_p , and ϑ are the transverse displacement, short circuit flexural rigidity, mass per unit area, and piezoelectric coupling of the plate, respectively; C_p is the piezoelectric capacitance of each unit cell; and the lattice coordinates (r, s) denote the unit cell whose origin is at a position $\mathbf{P}_{rs} = r\mathbf{a}_1 + s\mathbf{a}_2$, which has corresponding electrode voltage $v_{rs,0}(t)$ and current input $i_{rs}(t)$ (using the active sign convention). Furthermore, the electrode shape function $d(\mathbf{P})$

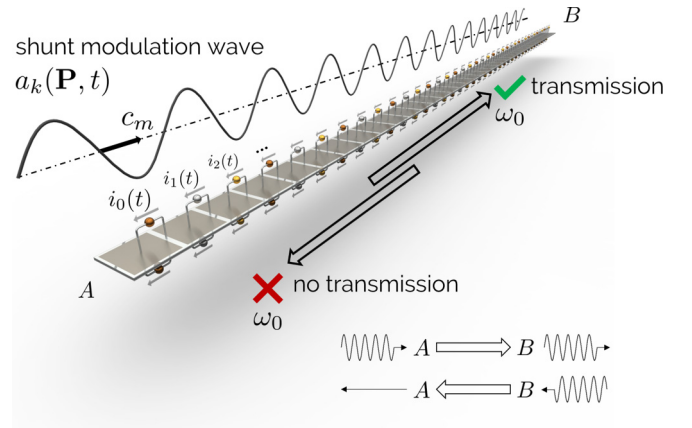


FIG. 2. Concept for a nonreciprocal piezoelectric metamaterial. Wavelike modulation of the shunt circuit coefficients $a_k(\mathbf{P}, t)$ results in transmission from A to B at frequency ω_0 , but no transmission from B to A.

is defined as

$$d(\mathbf{P}) = \begin{cases} 1, & \mathbf{P} \in D_0 \\ 0, & \text{otherwise,} \end{cases} \quad (3)$$

where $D_0 \subseteq D$ is the subdomain of the electrode in the unit cell at the origin, such that $d(\mathbf{P} - \mathbf{P}_{rs})$ defines the electrode of the unit cell at (r, s) . We neglect the mass and stiffness introduced by the thin metallic electrodes and associated wiring, making the assumption that the wires used are thin and flexible to reduce their effect on the system dynamics. Experimental realization of such a system will require wiring all electrodes to a dedicated circuit that supplies the current input $i_{rs}(t)$ for each electrode pair, but this circuit can be kept physically separate from the primary structure.

The current input $i_{rs}(t)$ in Eq. (2) is determined by the dynamics of the shunt circuit connected to the piezoelectric electrodes. We assume that each shunt circuit in the metamaterial has an identical layout with N circuit nodes (including the piezoelectric electrode pair), but with time-periodic components that can differ in phase. For a general shunt circuit with N nodes connected by time-varying components, application of Kirchoff's current law at each node yields an equation of the form

$$i_{rs}(t) \delta_{p,0} = \sum_{k,q} [A_k(\mathbf{P}_{rs}, t)]_{pq} v_{rs,q}^{(k)}(t), \quad (4)$$

where $(A_k)_{pq}$ are the elements of the the $N \times N$ coefficient matrix \mathbf{A}_k corresponding to the k th voltage derivative, and $v_{rs,q}$ are the node voltages. We assume the elements of $\mathbf{A}_k(\mathbf{P}, t)$ vary in a wavelike fashion, each with temporal period T_m and spatial period $\mathbf{P}_{r_m s_m}$, with $r_m, s_m \in \mathbb{Z}^+$. This modulation scheme is shown schematically in Fig. 2 for the case of a single-node system, in which case the matrix $\mathbf{A}_k(\mathbf{P}, t)$ becomes the scalar $a_k(\mathbf{P}, t)$.

The spatially discrete time-periodic coefficient matrices $\mathbf{A}_k(\mathbf{P}_{rs}, t)$ are sampled from the spatiotemporal periodic $\mathbf{A}_k(\mathbf{P}, t)$, which can be expanded as a Fourier series of the

form

$$\mathbf{A}_k(\mathbf{P}, t) = \sum_{l,m,n} \mathbf{C}_{klmn} e^{i(l\omega_m t - \tilde{\mathbf{G}}_{mn} \cdot \mathbf{P})} \quad (5)$$

with Fourier coefficients

$$\mathbf{C}_{klmn} = \langle e^{i(\tilde{\mathbf{G}}_{mn} \cdot \mathbf{P} - l\omega_m t)} \mathbf{A}_k(\mathbf{P}, t) \rangle, \quad (6)$$

where

$$\langle f(\mathbf{P}, t) \rangle \triangleq \frac{1}{r_m s_m T_m} \sum_{r=0}^{r_m-1} \sum_{s=0}^{s_m-1} \int_0^{T_m} f(\mathbf{P}_{rs}, t) dt \quad (7)$$

denotes the elementwise average over both space and time, and $\tilde{\mathbf{G}}_{mn} = m\tilde{\mathbf{b}}_1 + n\tilde{\mathbf{b}}_2$ is the (m, n) reciprocal lattice vector, where $\tilde{\mathbf{b}}_1$ and $\tilde{\mathbf{b}}_2$ are the reciprocal lattice vectors corresponding to the supercell lattice vectors $\tilde{\mathbf{a}}_1 = r_m \mathbf{a}_1$ and $\tilde{\mathbf{a}}_2 = s_m \mathbf{a}_2$ (see Fig. 1).

For a wave at frequency ω , it is hypothesized that the voltage on each electrode pair and associated circuit nodes will be harmonic at the wave frequency shifted by integer multiples of the modulation frequency ω_m , such that

$$v_{rs,q}(t) = e^{i\omega t} \sum_l V_{rslq}(\omega, \mathbf{k}) e^{il\omega_m t}. \quad (8)$$

Similarly, for a wave with Bloch wave vector \mathbf{k} , consider plane-wave solutions for the plate displacement $w(\mathbf{P}, t)$ of the form

$$w(\mathbf{P}, t) = e^{i(\omega t - \mathbf{k} \cdot \mathbf{P})} \sum_{l,m,n} W_{lmn}(\omega, \mathbf{k}) e^{i(l\omega_m t - \tilde{\mathbf{G}}_{mn} \cdot \mathbf{P})}. \quad (9)$$

The remainder of the analysis follows a typical plane-wave expansion procedure. Substituting Eqs. (8) and (9) into Eqs. (1) and (2) and applying the orthogonality of the complex exponentials, the following system of equations is obtained (in the following, dependence on ω and \mathbf{k} will be omitted for clarity):

$$\begin{aligned} & [D^E \|\mathbf{k} + \tilde{\mathbf{G}}_{mn}\|^4 - m_p(\omega + l\omega_m)^2] W_{lmn} \\ & - \vartheta \sum_{r=0}^{r_m-1} \sum_{s=0}^{s_m-1} \Gamma_{mnr s} V_{rslq} \delta_{q,0} = 0, \quad (10) \\ & [i(\omega + l\omega_m)] \left[C_p V_{rslu} + \vartheta \Delta \tilde{D} \sum_{m,n} \Gamma_{mnr s}^* W_{lmn} \right] \delta_{u,0} \\ & = \sum_{v,k,q,m,n} (C_{k,l-q,m,n})_{uv} e^{-i\tilde{\mathbf{G}}_{mn} \cdot \mathbf{P}_{rs}} [i(\omega + q\omega_m)]^k V_{rsqv}, \quad (11) \end{aligned}$$

where the coupling term $\Gamma_{mnr s}$ is given by

$$\Gamma_{mnr s} = \frac{1}{\Delta \tilde{D}} e^{i(\mathbf{k} + \tilde{\mathbf{G}}_{mn}) \cdot \mathbf{P}_{rs}} \int_{D_0} \nabla^2 e^{i(\mathbf{k} + \tilde{\mathbf{G}}_{mn}) \cdot \mathbf{P}} dD \quad (12)$$

and $\Delta \tilde{D} = \|\tilde{\mathbf{a}}_1 \times \tilde{\mathbf{a}}_2\| = r_m s_m \|\mathbf{a}_1 \times \mathbf{a}_2\|$ is the area of the supercell. Equations (10) and (11) form a rational eigenvalue problem [22] that can be used to solve for the dispersion relation for spatiotemporal periodic piezoelectric metamaterials. To solve the eigenvalue problem, the summations over the plane-wave indices (m, n) and the harmonic index q in Eqs. (10) and (11) must be truncated at some finite value. For maximum plane-wave index M and maximum harmonic index

L (i.e., $m, n \in [-M, M]$, $q \in [-L, L]$), with N total circuit nodes per shunt circuit, the system matrices are size

$$N_{\text{tot}} = [(2M + 1)^2 + r_m s_m N](2L + 1). \quad (13)$$

With this truncation, Eqs. (10) and (11) take the form

$$\mathbf{R}(\omega, \mathbf{k}) \mathbf{x} = \mathbf{0}, \quad (14)$$

where

$$\mathbf{R}(\omega, \mathbf{k}) = \mathcal{P}(\omega, \mathbf{k}) - \sum_{i=1}^k \frac{1}{d_i(\omega)} \mathbf{E}_i(\mathbf{k}). \quad (15)$$

Here, \mathcal{P} is an $N_{\text{tot}} \times N_{\text{tot}}$ matrix polynomial in ω , $d_i(\omega)$ are scalar polynomials that depend on the modulation scheme, and \mathbf{E}_i are coefficient matrices that depend only on the wave number \mathbf{k} . The order of the polynomial \mathcal{P} and the number of rational terms k depends on the modulation scheme. Note that this problem can be challenging to solve numerically in general (see, e.g., [22]), but many types of circuit modulation yield no rational terms, leaving a polynomial eigenvalue problem that is significantly easier to solve. For example, the use of inductive components will always generate rational terms in Eq. (15), because their current output depends on a voltage antiderivative. However, the use of fixed inductive components will yield only trivial rational terms with denominator $d_n(\omega) = \omega^n$, such that they can be multiplied through and included in the polynomial $\mathcal{P}(\omega, \mathbf{k})$.

Solving for the eigenfrequencies ω at each value of \mathbf{k} in the irreducible Brillouin zone yields the dispersion curves of the system. However, the introduction of time modulation generates additional copies of the dispersion branches at multiples of the modulation frequency ω_m , making it necessary to select only the physically relevant wave branches for plotting. Here we adopt the weighting method proposed by Vila *et al.* [12]. Each calculated (ω, \mathbf{k}) point is weighted by its corresponding zero-order plane-wave amplitude $|W_{000}(\omega, \mathbf{k})|$, which is assumed to be the leading term in the plane-wave expansion. For each value of \mathbf{k} , define the set of eigenvalues as $\Omega(\mathbf{k})$ and the corresponding eigenvectors as $X(\mathbf{k})$. For each eigenvalue $\omega_i \in \Omega(\mathbf{k})$ and the corresponding eigenvector $\mathbf{x}_i \in X(\mathbf{k})$, define the zero-order plane-wave component as $\alpha(\omega_i, \mathbf{k})$. Then, define the weighting

$$\sigma(\omega_i, \mathbf{k}) = \frac{|\alpha(\omega_i, \mathbf{k})|}{|\alpha_{\text{max}}(\mathbf{k})|} \quad (16)$$

where

$$|\alpha_{\text{max}}(\mathbf{k})| = \max_{\omega_i \in \Omega(\mathbf{k})} |\alpha(\omega_i, \mathbf{k})| \quad (17)$$

is the maximum fundamental wave amplitude over all of the eigenvectors of the resonant frequencies ω at the specified Bloch wave vector \mathbf{k} . The resulting points $[\mathbf{k}, \omega_i, \sigma(\omega_i, \mathbf{k})]$ are plotted as the dispersion curves, with a threshold on σ to highlight only the dominant wave modes. This methodology is numerically validated in a later case study through comparison of the predicted dispersion branches and the spectrum corresponding to time-domain simulation.

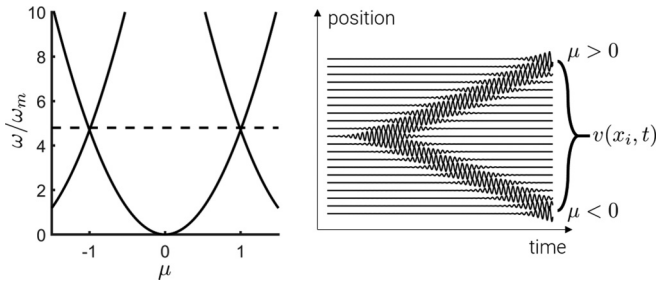


FIG. 3. Open circuit dispersion curve (left) and waterfall plot (right) of a representative transient response. The excitation center frequency is shown by the horizontal dashed line in the dispersion plot. The system does not exhibit a band gap, and so waves propagate symmetrically.

III. CASE STUDIES

Consider a 5 cm \times 5 cm square unit cell with an aluminum shim and PZT-5H piezoelectric layers, with parameters $D^E = 149.8$ Nm, $m_p = 17.7$ kg/m², $\vartheta = -0.047$ C. For concreteness, assume that each unit cell has a square electrode, with dimensions 4.5 cm \times 4.5 cm, centered in the unit cell, corresponding to capacitance $C_p = 78$ nF. To highlight the reciprocity breaking phenomenon, only modulation and wave propagation along the ΓX direction (i.e., along the x axis) is considered here. For waves propagating in this direction, the Bloch wave vector \mathbf{k} is given by $\mathbf{k} = \mu \hat{\mathbf{G}}_{10}$ where μ is a dimensionless normalized wave number. Due to the sign convention of Eq. (9), positive μ corresponds to waves propagating in the positive ΓX direction.

For implementation of these spatiotemporal periodic concepts in real systems, it is desirable to use the minimum required number of unit cells in the supercell without limiting performance. It has been noted in previous work that using two unit cells is insufficient to generate nonreciprocal behavior, since each modulated unit cell generates counterpropagating waves [17]. Thus, the results of this section consider a supercell of $r_m = 3$ and $s_m = 1$ unit cells along the x and y directions, respectively. Dispersion diagrams are calculated using Eqs. (10) and (11) by computing the eigenfrequencies ω at each value of μ . Time-domain results are obtained by direct integration (ode45 in Matlab) of Eqs. (1) and (2) using a Fourier discretization in space (periodic boundary conditions) and 904 primitive unit cells, large enough to prevent reflections at the domain edges. Note that the effect of varying the number of unit cells per supercell can be quantified using this framework (analogous to similar studies by the authors [21,23]), which may be of interest for controlling the scattering band-gap center frequency.

First, the baseline dispersion curves and transient response are examined with all of the shunt circuits at open circuit, with results shown in Fig. 3. The dispersion curves exhibit the expected reciprocal behavior, i.e., the curves are symmetric about the $\mu = 0$ axis. The transient simulation results are summarized using a waterfall plot, which shows the velocity time history $v(x_i, t)$ at various positions x_i along the propagation direction. The waterfall plots show that the input at the center generates symmetrically propagating waves corresponding to the $\mu > 0$ and $\mu < 0$ dispersion branches.

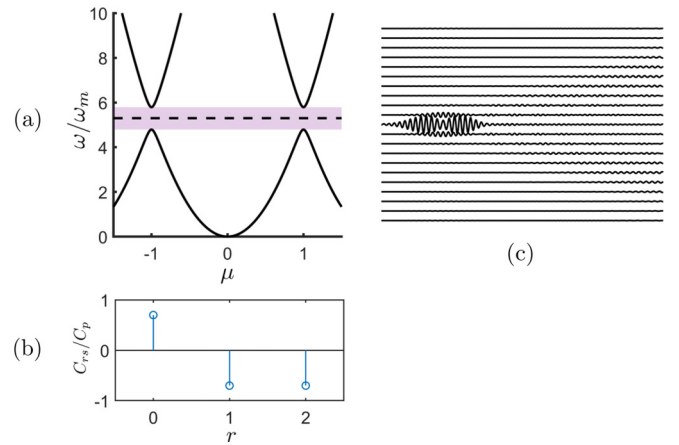


FIG. 4. (a) Dispersion curve corresponding to spatial capacitive modulation shown in (b). The excitation center frequency is shown by the horizontal dashed line in (a), yielding the waterfall plot in (c). As shown by the waterfall plot, all wave propagation is prevented within the band gap.

A. Capacitive spatiotemporal modulation

Capacitive loading results in a change to the piezoelectric metamaterial's static stiffness [21], with no frequency dependence. As such, spatial variation of shunt capacitance is analogous to a static, periodic variation in structure stiffness, which generates the well-known Bragg band gap [24,25] at the $\mu = \pm 1$ points of the dispersion curve. This dispersion behavior is illustrated in Fig. 4, together with the waterfall plot showing that waves do not propagate within the band gap.

Next, we consider a single-node shunt circuit with time-varying capacitance (e.g., a moving-plate parallel plate capacitor), with current given by

$$i_{rs}(t) = C_{rs}(t) \frac{dv_{rs,0}}{dt} + \frac{dC_{rs}}{dt} v_{rs,0}(t). \quad (18)$$

We consider both smooth sinusoidal capacitive modulation

$$C_{rs}(t) = C_0 + \Delta C \cos\left(\omega_m t - \frac{2\pi r}{r_m}\right) \quad (19)$$

and square-wave modulation

$$C_{rs}(t) = C_0 + \Delta C \operatorname{sgn}\left[\cos\left(\omega_m t - \frac{2\pi r}{r_m}\right)\right] \quad (20)$$

representative of switching the shunt capacitance between two values, $C_0 + \Delta C$ and $C_0 - \Delta C$. Dispersion curves and waterfall plots are shown in Figs. 5 and 6 for sinusoidal and square modulation, respectively, highlighting the resulting nonreciprocal behavior.

Figure 5 shows that sinusoidal spatiotemporal modulation of the shunt capacitance generates two direction-dependent band gaps, denoted by the red and blue shaded regions in Fig. 5(a). Note that the bandwidth of each band gap depends largely on the extent of negative capacitance used in the modulation, as this determines the extent of the effective stiffness modulation in the system. The shift in each band gap is approximately $\omega_m/2$, and the band gap in the same direction as the modulation wave (i.e., the $+\mu$ band gap) shifts upward, in agreement with previously obtained results

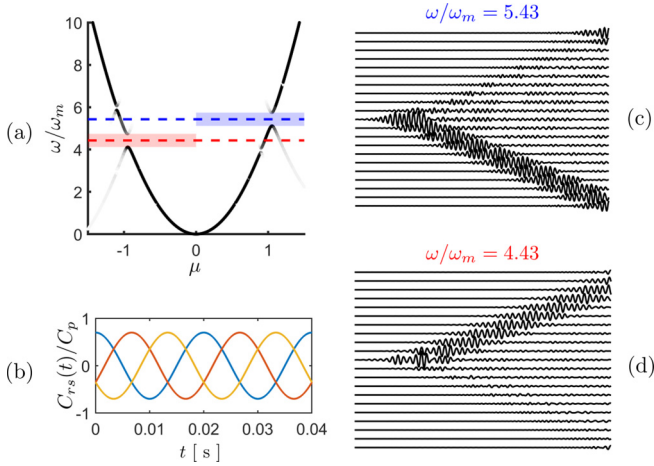


FIG. 5. (a) Dispersion curves for sinusoidal spatiotemporal modulation of shunt capacitance (b), with $C_0 = 0$, $\Delta C = 0.7C_p$, $\omega_m/(2\pi) = 50$ Hz. (c) Waterfall plot for a center frequency of $\omega/\omega_m = 5.43$ [blue horizontal dashed line in (a)], showing propagation in the $-\mu$ direction only. (d) Waterfall plot for a center frequency of $\omega/\omega_m = 4.43$ [red horizontal dashed line in (a)], showing propagation in the $+\mu$ direction only.

for spatiotemporal periodic systems [10]. The bandwidths of the upper and lower nonreciprocal band gaps are 31.25 and 31.15 Hz, respectively.

Square modulation results in qualitatively similar behavior to sinusoidal modulation, but may be more practical to implement using switching circuits. The bandwidths of the upper and lower nonreciprocal band gaps are 46.5 and 46 Hz, respectively. Note that the band gaps generated by square modulation (Fig. 6) have greater bandwidth than the equivalent sinusoidal modulation case (Fig. 5), due to the larger capacitance mismatch between adjacent unit cells.

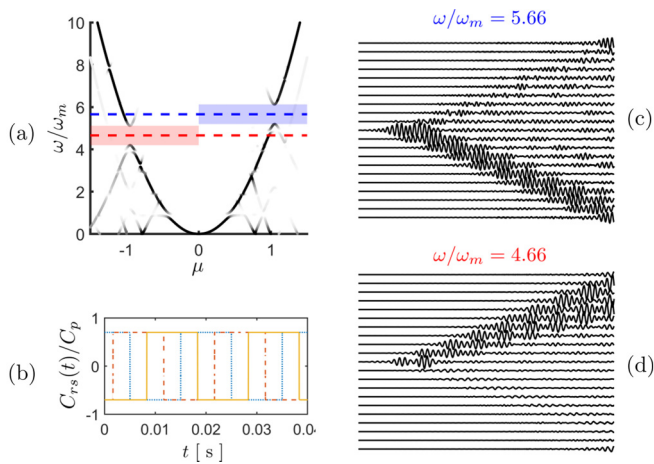


FIG. 6. (a) Dispersion curves for square-wave spatiotemporal modulation of shunt capacitance (b), with $C_0 = 0$, $\Delta C = 0.7C_p$, and $\omega_m/(2\pi) = 50$ Hz. (c) Waterfall plot for a center frequency of $\omega/\omega_m = 5.66$ [blue horizontal dashed line in (a)], showing propagation in the $-\mu$ direction only. (d) Waterfall plot for a center frequency of $\omega/\omega_m = 4.66$ [red horizontal dashed line in (a)], showing propagation in the $+\mu$ direction only.

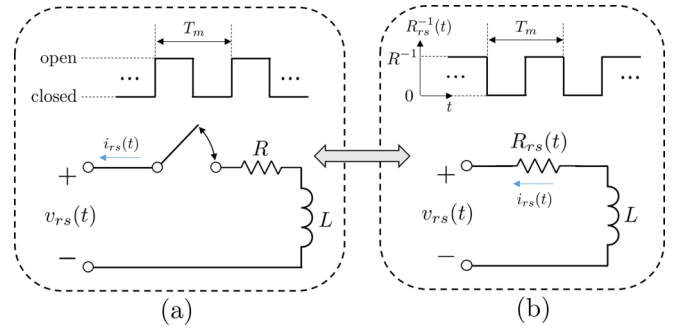


FIG. 7. (a) Schematic of the modulated inductive circuit and (b) its equivalent representation with a single time-varying resistor. The switch is periodically opened and closed at the modulation frequency $\omega_m = 2\pi/T_m$. The wiring resistance R is assumed to be small and is included to avoid singularities at short circuit.

B. Inductive spatiotemporal modulation

The mathematical framework presented here enables an analysis of fully general time-varying circuit networks with multiple nodes. Such systems have the potential to enable wave reciprocity breaking without using negative capacitance, which is associated with many practical stability challenges. To illustrate this point, we consider a circuit with a static inductance that is periodically connected and disconnected from the piezoelectric electrodes as shown in Fig. 7.

For convenience, we replace the switch and resistance R with a single time-varying resistor $R_{rs}(t)$, which switches between the wiring resistance R and open circuit. The current output from the circuit in Fig. 7(b) is given by

$$\begin{bmatrix} i_{rs} \\ 0 \end{bmatrix} = \frac{1}{R_{rs}(t)} \begin{bmatrix} -1 & 1 \\ -1 & 1 \end{bmatrix} \begin{bmatrix} v_{rs,0} \\ v_{rs,1} \end{bmatrix} + \frac{1}{L} \begin{bmatrix} 0 & 0 \\ 0 & 1 \end{bmatrix} \begin{bmatrix} v_{rs,0} \\ v_{rs,1} \end{bmatrix}^{(-1)}, \quad (21)$$

where $v_{rs,1}$ is the voltage across the inductor. For a given admittance function $Y_{rs}(t) = 1/R_{rs}(t)$, substituting Eq. (21) into Eqs. (6), (10), and (11) yields a quadratic eigenvalue problem that can be solved for the dispersion characteristics of this system. For concreteness, we consider circuit parameters $R = 100 \Omega$ and $L = 2.65$ H, corresponding to an undamped electrical resonant frequency of $\omega_r/(2\pi) = 350$ Hz while the switch is closed. To facilitate time-domain numerical integration, a differentiable approximation to a square switching function is used, i.e.,

$$Y_{rs}(t) = \frac{1}{2R} + \frac{1}{\pi R} \tan^{-1} \left[\frac{1}{\delta} \cos \left(\omega_m t - \frac{2\pi r}{r_m} \right) \right], \quad (22)$$

where δ is a small parameter that determines the sharpness of the transition from open circuit to the short circuit resistance R .

With modulation in space only (i.e., $\omega_m = 0$), this system exhibits both a locally resonant band gap near the resonant frequency ω_r and a scattering band gap due to the stiffness mismatch between shunted and open circuit unit cells. The dispersion and waterfall plots for the spatially periodic inductive system are shown in Fig. 8 for the case of a single connected inductor and two disconnected inductors. Waves are strongly attenuated in both band gaps.

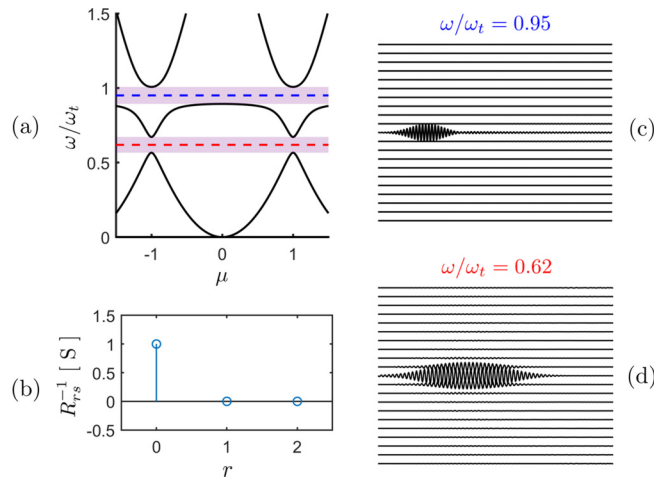


FIG. 8. (a) Dispersion curves for spatial inductive modulation using the modulated resistance shown in (b). This system exhibits both a locally resonant band gap (c) that occurs at $\omega/\omega_t = 0.95$ and a scattering band gap (d) at $\omega/\omega_t = 0.62$. As shown by the waterfall plots, propagation is prevented in both band gaps.

To break reciprocity in the inductive system, we introduce temporal modulation at a frequency $\omega_m/(2\pi) = 30$ Hz with switching parameter $\delta = 10^{-6}$. Additionally, a constant resistance $R_b = 1 \text{ M}\Omega$ is placed between the piezoelectric electrodes and ground and between the two terminals of the inductor to improve numerical stability. Dispersion predictions and transient simulation results are shown in Fig. 9.

The developed plane-wave expansion technique yields dispersion curves that closely match the transient simulation results, validating the weighting technique described in Sec. II for plotting a single dispersion curve in the time-modulated system. Introducing spatiotemporal switching into the inductive system breaks wave reciprocity at the scattering band gap, shifting the band gaps as with the previously shown cases of capacitive modulation. The bandwidths of the upper and lower nonreciprocal band gaps are 28.1 and 29 Hz, respectively. Importantly, this modulation scheme requires only a fixed inductance and switching circuit. For such systems, the effective material property description becomes less effective, as it is unclear how frequency-dependent effective properties change under time modulation.

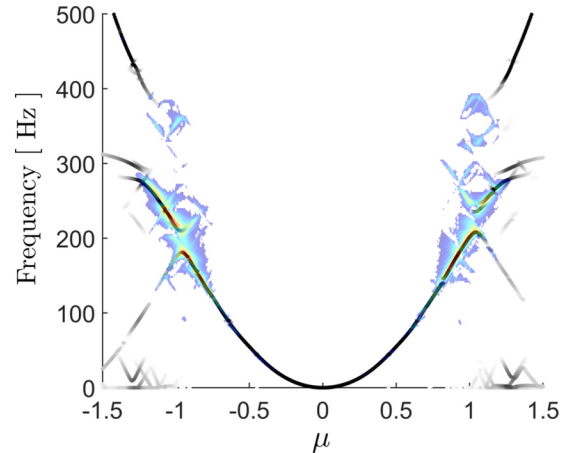


FIG. 9. Plane-wave expansion dispersion curves (solid lines) and transient simulation two-dimensional fast Fourier transform (heatmap) for switched inductive loading. For the plane-wave expansion method, $L = 13$ and $M = 1$ harmonics were used. Nonreciprocal behavior is observed at the scattering band gaps near $\mu = \pm 1$. There is excellent agreement between the plane-wave expansion predictions and the transient simulations.

IV. CONCLUSIONS

We introduce a fully coupled electromechanical framework to enable nonreciprocal piezoelectric metamaterials. By including circuit dynamics directly, the developed model captures the reciprocity-breaking phenomenon without relying on the assumption of modulated equivalent material properties. Specifically, a generalized electromechanical plane-wave expansion method is presented for analyzing the dispersion relations of piezoelectric metamaterial plates with time- and space-modulated shunt circuits. It is shown that the most general case of spatiotemporal periodic modulation of shunt circuit parameters yields a rational eigenvalue problem. Case studies demonstrate that spatiotemporal modulation of capacitance can break reciprocity and create unidirectional band gaps. Importantly, it is demonstrated that switched inductive loading is sufficient to break wave reciprocity, avoiding the power consumption and stability issues associated with negative capacitance. Additionally, the developed framework can describe modulation schemes with no clear effective material property representation, as in the case of frequency-dependent effective properties.

[1] Z. Yu and S. Fan, Complete optical isolation created by indirect interband photonic transitions, *Nat. Photonics* **3**, 91 (2009).
 [2] S. A. Cummer, J. Christensen, and A. Alù, Controlling sound with acoustic metamaterials, *Nat. Rev. Mater.* **1**, 16001 (2016).
 [3] A. Maznev, A. Every, and O. Wright, Reciprocity in reflection and transmission: What is a “phonon diode”?, *Wave Motion* **50**, 776 (2013).
 [4] B.-I. Popa and S. A. Cummer, Non-reciprocal and highly nonlinear active acoustic metamaterials, *Nat. Commun.* **5**, 3398 (2014).

[5] J. Zhang, B. Peng, Ş. K. Özdemir, Y.-x. Liu, H. Jing, X.-y. Lü, Y.-l. Liu, L. Yang, and F. Nori, Giant nonlinearity via breaking parity-time symmetry: A route to low-threshold phonon diodes, *Phys. Rev. B* **92**, 115407 (2015).
 [6] R. Fleury, D. L. Sounas, C. F. Sieck, M. R. Haberman, and A. Alù, Sound isolation and giant linear nonreciprocity in a compact acoustic circulator, *Science* **343**, 516 (2014).
 [7] Y. Chen, X. Li, H. Nassar, G. Hu, and G. Huang, A programmable metasurface for real time control of broadband elastic rays, *Smart Mater. Struct.* **27**, 115011 (2018).

- [8] Y. Zhai, H.-S. Kwon, and B.-I. Popa, Active Willis metamaterials for ultracompact nonreciprocal linear acoustic devices, *Phys. Rev. B* **99**, 220301(R) (2019).
- [9] M. Brandenbourger, X. Locsin, E. Lerner, and C. Coulais, Non-reciprocal robotic metamaterials, *Nat. Commun.* **10**, 1 (2019).
- [10] G. Trainiti and M. Ruzzene, Non-reciprocal elastic wave propagation in spatiotemporal periodic structures, *New J. Phys.* **18**, 083047 (2016).
- [11] D. L. Sounas and A. Alù, Non-reciprocal photonics based on time modulation, *Nat. Photonics* **11**, 774 (2017).
- [12] J. Vila, R. K. Pal, M. Ruzzene, and G. Trainiti, A Bloch-based procedure for dispersion analysis of lattices with periodic time-varying properties, *J. Sound Vib.* **406**, 363 (2017).
- [13] H. Nassar, X. Xu, A. Norris, and G. Huang, Modulated phononic crystals: Non-reciprocal wave propagation and Willis materials, *J. Mech. Phys. Solids* **101**, 10 (2017).
- [14] H. Nassar, H. Chen, A. Norris, M. R. Haberman, and G. Huang, Non-reciprocal wave propagation in modulated elastic metamaterials, *Proc. R. Soc. A: Math., Phys. Eng. Sci.* **473**, 20170188 (2017).
- [15] C. Shen, X. Zhu, J. Li, and S. A. Cummer, Nonreciprocal acoustic transmission in space-time modulated coupled resonators, *Phys. Rev. B* **100**, 054302 (2019).
- [16] G. W. Milton, M. Briane, and J. R. Willis, On cloaking for elasticity and physical equations with a transformation invariant form, *New J. Phys.* **8**, 248 (2006).
- [17] E. Riva, J. Marconi, G. Cazzulani, and F. Braghin, Generalized plane wave expansion method for non-reciprocal discretely modulated waveguides, *J. Sound Vib.* **449**, 172 (2019).
- [18] M. Ansari, M. Attarzadeh, M. Nough, and M. A. Karami, Application of magnetoelastic materials in spatiotemporally modulated phononic crystals for nonreciprocal wave propagation, *Smart Mater. Struct.* **27**, 015030 (2017).
- [19] G. Trainiti, Y. Xia, J. Marconi, G. Cazzulani, A. Erturk, and M. Ruzzene, Time-Periodic Stiffness Modulation in Elastic Metamaterials for Selective Wave Filtering: Theory and Experiment, *Phys. Rev. Lett.* **122**, 124301 (2019).
- [20] C. Sugino, M. Ruzzene, and A. Erturk, Design and analysis of piezoelectric metamaterial beams with synthetic impedance shunt circuits, *IEEE/ASME Trans. Mech.* **23**, 2144 (2018).
- [21] C. Sugino, M. Ruzzene, and A. Erturk, An analytical framework for locally resonant piezoelectric metamaterial plates, *Int. J. Solids Struct.* **182**, 281 (2020).
- [22] Y. Su and Z. Bai, Solving rational eigenvalue problems via linearization, *SIAM J. Matrix Anal. Appl.* **32**, 201 (2011).
- [23] C. Sugino, S. Leadenham, M. Ruzzene, and A. Erturk, An investigation of electroelastic bandgap formation in locally resonant piezoelectric metastructures, *Smart Mater. Struct.* **26**, 055029 (2017).
- [24] M. S. Kushwaha, P. Halevi, L. Dobrzynski, and B. Djafari-Rouhani, Acoustic Band Structure of Periodic Elastic Composites, *Phys. Rev. Lett.* **71**, 2022 (1993).
- [25] V. Laude, *Phononic crystals*, De Gruyter Studies in Mathematical Physics Vol. 26 (Walter de Gruyter GmbH, Berlin, Germany, 2015).